Geophysical Journal International

Geophys. J. Int. (2016) **205,** 236–242
GJI Gravity, geodesy and tides

doi: 10.1093/gji/ggw016

An improved geodetic source model for the 1999 M_w 6.3 Chamoli earthquake, India

Wenbin Xu,[1,2] Roland Bürgmann[1] and Zhiwei Li[2]

[1]*Department of Earth and Planetary Science, University of California, Berkeley, California, USA. E-mail: wenbin.xu@kaust.edu.sa*
[2]*School of Geosciences and Info-Physics, Central South University, Changsha* 410083, *Hunan, China*

Accepted 2016 January 11. Received 2016 January 9; in original form 2015 August 28

SUMMARY

We present a distributed slip model for the 1999 M_w 6.3 Chamoli earthquake of north India using interferometric synthetic aperture radar (InSAR) data from both ascending and descending orbits and Bayesian estimation of confidence levels and trade-offs of the model geometry parameters. The results of fault-slip inversion in an elastic half-space show that the earthquake ruptured a $9^{\circ}{}^{+3.4}_{-2.2}$ northeast-dipping plane with a maximum slip of ∼1 m. The fault plane is located at a depth of $\sim 15.9^{+1.1}_{-3.0}$ km and is ∼120 km north of the Main Frontal Thrust, implying that the rupture plane was on the northernmost detachment near the mid-crustal ramp of the Main Himalayan Thrust. The InSAR-determined moment is 3.35×10^{18} Nm with a shear modulus of 30 GPa, equivalent to M_w 6.3, which is smaller than the seismic moment estimates of M_w 6.4–6.6. Possible reasons for this discrepancy include the trade-off between moment and depth, uncertainties in seismic moment tensor components for shallow dip-slip earthquakes and the role of earth structure models in the inversions. The released seismic energy from recent earthquakes in the Garhwal region is far less than the accumulated strain energy since the 1803 M_s 7.5 earthquake, implying substantial hazard of future great earthquakes.

Key words: Radar interferometry; Earthquake source observations; Crustal structure; Asia.

1 INTRODUCTION

The Himalayan range formed due to the collision of the Indian plate and southern Tibet. Recent GPS-constrained convergence rates range from ∼13.3 ± 1.7 mm yr^{-1} in northwest India to ∼21.2 ± 2.0 mm yr^{-1} in Assam (Stevens & Avouac 2015). As a result of the crustal shortening, several thrust faults have developed in the Himalayan range, such as the Main Central Thrust (MCT), the Main Boundary Thrust (MBT) and the Main Frontal Thrust (MFT). Currently, most slip appears to involve the MFT (Lavé & Avouac 2001), but there is geologic evidence for some out-of-sequence faulting further north (e.g. Wobus *et al.* 2005). These faults cut the entire crust independently but are rooted into a common basal detachment termed the Main Himalayan Thrust (MHT; Ni & Barazangi 1984; Yin 2006), which has a flat-ramp-flat geometry. Recent geodetic observations using interseismic coupling models reveal that the MHT is fully locked from the frontal flat to the mid-crustal ramp at ∼20 km depth (Feldl & Bilham 2006; Ader *et al.* 2012; Avouac 2015; Stevens & Avouac 2015). As slip deficit and stress are accumulating on the fault ramp, this portion of the MHT has the potential to generate great earthquakes and is also responsible for mountain building (Banerjee & Bürgmann 2002; Grandin *et al.* 2012).

The Garhwal region lies in an 800-km-long seismic gap between the rupture zones of the 1905 M_s 7.8 Kangra and 1934 M_w 8 Bihar earthquakes, where great earthquakes have rarely occurred during the past ∼500 years (Rajendran *et al.* 2015). GPS measurements indicate that the region may have a slip potential of nearly 10 m, implying that the moment deficit and equivalent magnitude of a gap-filling event can be greater than 8.5 (Bilham *et al.* 2001). Recently, the M_w 7.8 Gorkha, Nepal earthquake took place in the eastern section of this seismic gap, causing significant damage and casualties (Avouac *et al.* 2015; Galetzka *et al.* 2015; Lindsey *et al.* 2015; Wang & Fialko 2015). To the west, the Garhwal region has experienced several moderate-sized earthquakes in the 1990 s, the most prominent being the 1991 M_w 6.8 Uttarkashi and the 1999 M_w 6.3 Chamoli earthquakes.

In this work, we focus on the Chamoli earthquake that occurred on 1999 March 29. The main shock was widely felt in Uttarakhand, damaging tens of thousands of houses and causing ∼103 casualties (Sarkar *et al.* 2001). No apparent foreshocks had been recorded prior to the main shock, but intense aftershocks have been observed, including several events with $M_w > 5$. Most of the aftershocks were located to the east of Chamoli village (Fig. 1). The 1999 Chamoli earthquake has been studied using geodetic and seismic methods (Mukhopadhyay & Kayal 2003; Rajput *et al.* 2005; Satyabala &

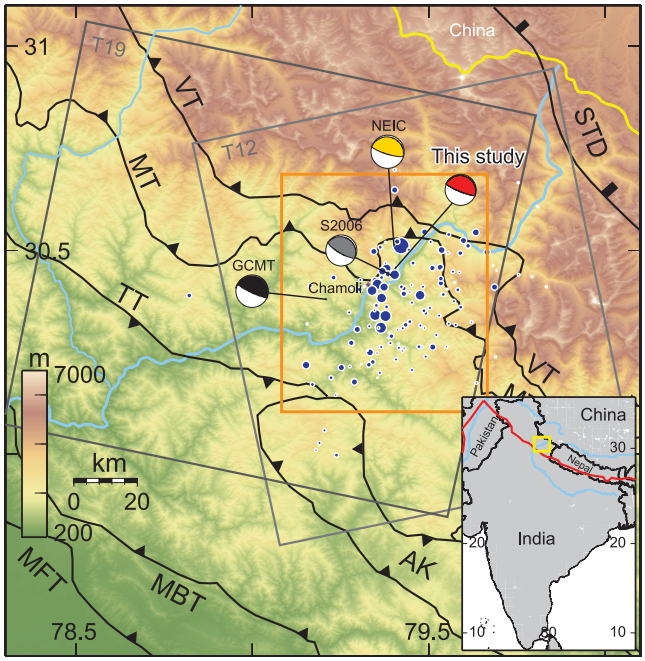

Figure 1. Location of the 1999 Chamoli earthquake in north India. Blue dots represent the earthquakes recorded by the International Seismological Centre (ISC) in 1999 and the focal mechanisms indicate main-shock locations from the different seismic catalogues in comparison to our study, S2006: Satyabala & Bilham (2006). Mapped thrust faults are shown in black: MFT, Main Frontal Thrust; MBT, Main Boundary Thrust; TT, Tons Thrust; AK, Almora Klippe; MT, Munsiari Thrust; VT, Vaikrita Thrust; STD, South Tibet Detachment (Lavé & Avouac 2001; Célérier *et al.* 2009). Two main rivers are shown in light blue. Grey boxes outline ascending and descending orbit SAR frames, respectively. The yellow box in the inset map shows the location of Fig. 1. The orange rectangle outlines the study area in Figs 2 and 3.

Bilham 2006), but whether the source fault of the main shock was on the MHT has not been unambiguously resolved. Using data from the European Space Agency's European Remote Sensing satellites ERS-1/2 from both ascending and descending orbits, Satyabala & Bilham (2006) observed more than two fringes of ground deformation (line-of-sight displacement ∼6 cm) in the interferograms from both orbits. Their uniform-slip model suggests that the source fault had a strike of N300°W and dips 15° to the northeast. Due to the incomplete ground deformation maps, Satyabala & Bilham (2006) argued that their modelling results were non-unique and found that a range of dips and depths could fit the data. Therefore, their results did not provide a good understanding of the causative fault and rupture processes involved in generating the 1999 Chamoli earthquake. Through inversion of seismic phase data, Mukhopadhyay & Kayal (2003) argued that the earthquake took place on the MHT. In this study, we reprocess the ERS 1/2 data using a different strategy to generate better-quality interferograms. We then invert for a finite-fault slip model of the 1999 Chamoli earthquake and use Bayesian estimation to generate confidence levels and trade-offs between the estimated model parameters. We suggest the 1999 Chamoli earthquake occurred on the mid-crustal ramp of the MHT.

2 InSAR OBSERVATIONS

Similar to Satyabala & Bilham (2006), we use the ascending and descending C-band (5.6 cm wavelength) InSAR data from the ERS 1/2 to investigate the coseismic ground deformation with the method of two-pass differential interferometry. We process the data with the GAMMA software and use the 1 arc s^{-1} Shuttle Radar Topography Mission digital elevation model (Farr *et al.* 2007) to simulate and eliminate the topographic signals. To increase the signal-to-noise ratio (SNR), the interferograms are multi-looked to about 160-m pixel spacing. Layover and shadowing from rough mountain topography make phase unwrapping in the radar coordinate system difficult. To overcome this issue, we first geocode the interferograms from the radar coordinate system into a geographic one (WGS84) and filter them with the improved Goldstein filter (Li *et al.* 2008). The geocoded interferograms are then unwrapped using the minimum cost flow method (Chen & Zebker 2001). We remove a ramp associated with the orbital error across the unwrapped interferogram for track 12. We do not remove elevation-dependent atmospheric effects, as they are not substantially affecting either interferogram. Finally, we carefully check the results of phase unwrapping and mask out areas with low coherence in which some remaining unwrapping errors are evident (see Supporting Information Fig. S1, available in the electronic supplement). We crop out the ∼30 km by ∼45 km deforming area for further analysis.

Compared to Satyabala & Bilham (2006), our surface displacement measurements provide a more complete ground deformation field for both the ascending and descending orbits (Figs 2 and 3). The major deformation signals are confined to a region of ∼1350 km^2. The maximum displacement in the radar line-of-sight direction (LOS) is ∼8 cm near Chamoli village and south of the surface trace of the Munsiari Thrust (MT). Clear range-increase signals of ∼2 cm in LOS are observed north of the maximum uplift in both ascending and descending orbits, indicating subsidence of similar magnitude. These deformation signals are consistent with what would be expected from a thrust-faulting earthquake.

3 FINITE SLIP MODEL

With observations from both ascending and descending orbits, we determine a finite-fault slip model and evaluate the uncertainties of the model parameters. We use a single rectangular dislocation (Okada 1985) in a homogeneous and isotropic elastic Poisson half-space (Poisson's ratio $\nu = 0.25$). We subsample our data points using the quadtree method (Jónsson *et al.* 2002). We use an exponential covariance function to empirically estimate the noise distribution of the interferogram (Sudhaus & Jónsson 2009). The estimated data covariance function for the ascending data is: $C_{\mathrm{asc}}(h) = 25 - (26 \cdot (1 - e^{-\frac{h}{6.97}}))$ and for the descending data is $C_{\mathrm{desc}}(h) = 62 - (86 \cdot (1 - e^{-\frac{h}{36.13}}))$, respectively (see Supporting Information Fig. S2, available in the electronic supplement). We use these covariance functions to build the data covariance matrix and to weight the data in the optimization. We fix the rake to be 90° (pure thrust) and find the optimal fault model parameters with uniform thrust slip using a Monte Carlo-type simulated annealing algorithm, followed by a gradient-based iterative method (Cervelli *et al.* 2001). Our optimal model fault is northeasterly dipping at an angle of $9^{\circ}{}^{+3.4}_{-2.2}$, with a $\mathrm{N292}^{\circ}{}^{+5.1}_{-3.4}$ W orientation with its upper and lower edges at ∼15 and ∼16 km depth, respectively.

To determine finer details of the thrust-slip distribution, we fix the strike and dip of the fault plane, extend the length of the fault to 30 km along strike and the width to 20 km and then discretize the fault plane into 1 km × 1 km patches. To prevent oscillatory solutions, the inversion is regularized with smoothness constraints (Jónsson *et al.* 2002). Our final thrust-slip solution shows that the predicted ground displacements fit the observations well (Figs 2

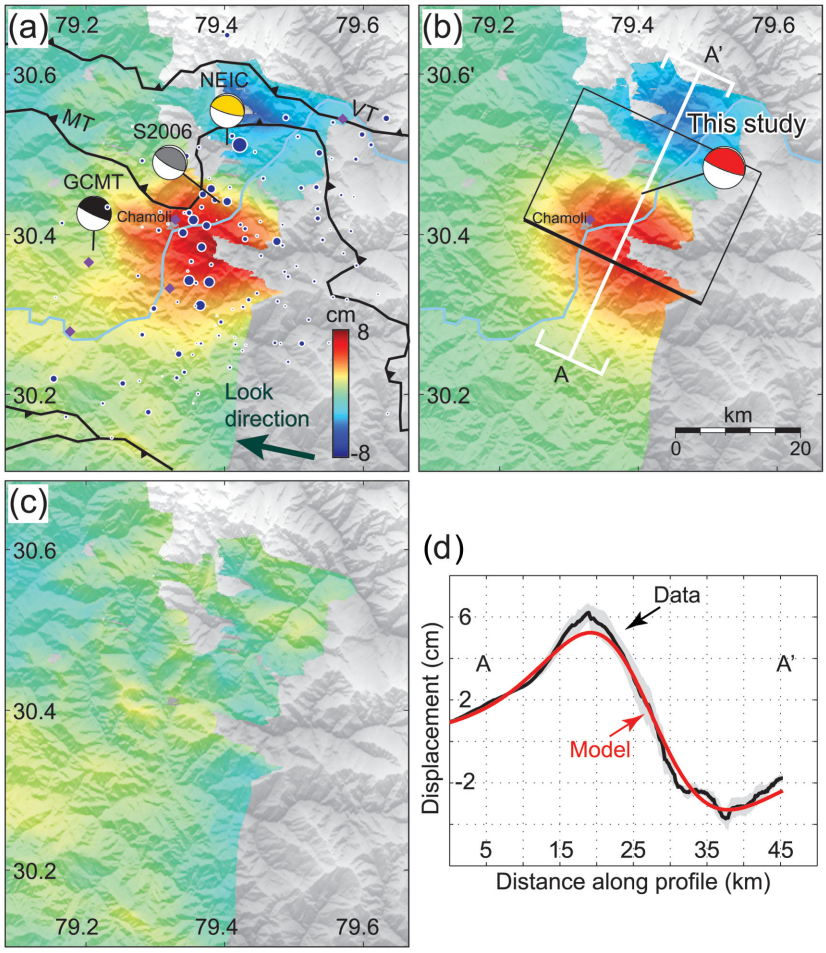

Figure 2. Coseismic InSAR data of the 1999 Chamoli earthquake and the modelling result. (a) Observed LOS displacement map from the descending ERS-2 satellite track 19, with positive values indicating ground movement towards the satellite (primarily uplift). (b) Model prediction for panel (a) with the surface projection of the estimated fault plane indicated by a black rectangle (upper edge in bold). (c) Residual. (d) Observed (black) and modelled (red) displacements along profiles A–A′ in panel (b). The scale is the same for all panels.

and 3). We believe that the residuals are likely due to atmospheric artefacts and the model simplifications (i.e. single planar fault surface, smoothed slip distribution) (Qiao *et al.* 2010; Xu *et al.* 2010). The RMS of the misfit between the InSAR data and the model prediction is 0.6 cm for both the ascending and descending orbits. The fault slip distribution is symmetric and is concentrated at depths between ∼15.2 km and ∼17 km, with a central slip maximum of ∼1 m at a depth of 16.2 km, ∼120 km north of the MFT (Fig. 4). The centroid depth estimated from our InSAR inversion model is 15.9 km. Very little slip is found below 17.4 km depth. Assuming a shear modulus of $\mu = 30$ GPa, the estimated geodetic moment is 3.35×10^{18} Nm, corresponding to $M_w = 6.3$.

We use the Bayesian estimation to determine the model parameter uncertainties (Xu *et al.* 2015). The prior probability density function of the source parameters is assumed to be a uniform distribution. The resulting marginal distributions of the model parameters from the Bayesian estimation show that they are well constrained (Table 1). The optimal values of the model parameters correlate well with the peaks of the Bayesian estimation. The 2-D distribution of the model parameters clearly shows the trade-offs between fault width, fault depth and magnitude of the event (Fig. 4). In particular, deeper model ruptures require somewhat larger magnitudes. Except for fault dip and strike, the best-fit model parameters by Satyabala & Bilham (2006) are located within the 95 per cent confidence intervals (Table 1). The optimal model parameters together with several solutions derived from previous studies (i.e. National Earthquake Information Center, NEIC; Global Centroid Moment Tensor, GCMT; and S2006) can also be found in Table 1. The fault strike and dip reported in the seismic catalogues fall outside the 95 per cent confidence intervals as estimated by InSAR.

4 DISCUSSION

How and where recent moderate to great earthquakes nucleate and propagate in the Himalayan range has been long debated. Some argue that they rupture the locked detachment within the MHT (Avouac *et al.* 2015; Galetzka *et al.* 2015), while others suggest that they can be located on secondary splay faults above the MHT (Wobus *et al.* 2005). Geologic and geomorphic evidence indicate that the dip of the locked section increases smoothly from 4° at shallow depth to 9° at ∼20 km depth (Cattin & Avouac 2000; Grandin *et al.* 2012). Inversion of geodetically measured ground deformation associated with the 2015 M_w 7.8 Gorkha earthquake show that the shallow flat section and the mid-crustal ramp on the

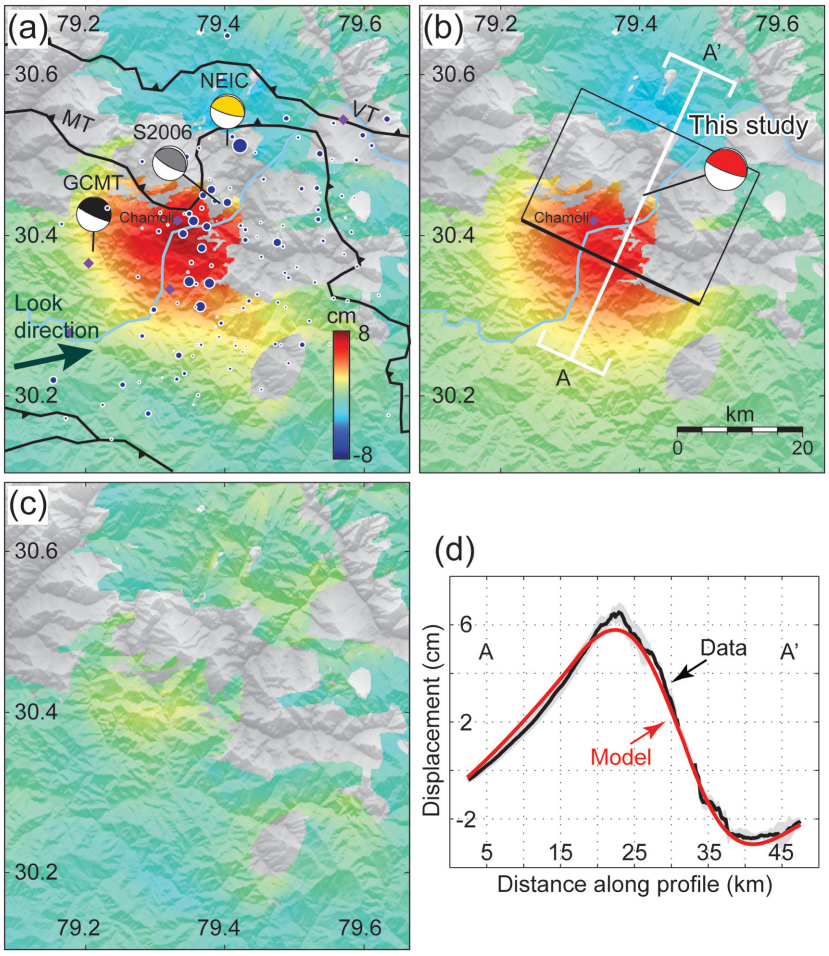

Figure 3. Same as Fig. 2, but from the ascending ERS-1/2 satellites track 12.

MHT are dipping 7° and 20° to the north, respectively (Elliot *et al.* 2015; Feng *et al.* 2015). In the Garhwal region, seismic images indicate that the location of the ramp is ∼120 km from the surface trace of the MFT at a depth of 10–20 km, the upper flat dips at 2° and the ramp dips at 16° (Caldwell *et al.* 2013). Our inversion results suggest that the rupture plane of the 1999 Chamoli earthquake is located ∼120 km north of the MFT at $15.9^{+1.1}_{-3.0}$ km depth and dipping $9^{\circ+3.4}_{-2.2}$ towards the northeast. Together with previous studies, our modeling results indicate that the earthquake extended down the ramp of the MHT.

The greater than two-fold difference in seismic and geodetic moment estimates for the Chamoli earthquake may be due to biases affecting either approach. With increasing source depth, the SNR decreases for the surface displacement measurements. The data are also decorrelated near the epicentre and the northeast part of the fault rupture, which could lead to the underestimation of the earthquake magnitude. Consideration of parameter trade-offs in our inversion (Fig. 4) shows that only a modest covariance of dislocation depth and M_w, with ∼2-km-deeper models allowing for M_w increases of ∼0.04. Generally, geodetic data are modelled in a half-space using classical elastic dislocation theory (Okada 1985), while local 1-D (or global 3-D) earth structure are taken into account when modelling seismic data. In geodetic models employing a layered earth structure with elastic moduli increasing with depth, more slip is required in the higher-rigidity material at depth to produce the observed surface displacements and earthquake magnitude estimates are increased (e.g. Hearn & Bürgmann 2005). Half-space model inversions also tend to underestimate the depth of earthquakes by 10–30 per cent (e.g. Weston *et al.* 2011). Statistic comparison between seismically and geodetically derived seismic moments of 96 earthquakes suggests that there is a slight tendency of InSAR-derived models predicting smaller seismic moments than those reported in the GCMT catalogue (Weston *et al.* 2011). They also found that the difference of seismic moment can sometime reach 50 per cent. Weston *et al.* (2011) also found that the difference of earthquake moment estimates can sometimes be as large as a factor of two (see their fig. 4a).

To investigate the influence of using a layered model, we calculate a forward model using the PSGRN/PSCMP program from Wang *et al.* (2006; Fig. 5a). We run the forward model using our preferred slip distribution and the local 1-D structure from Galetzka *et al.* (2015). This 1-D model has four different shear moduli within 27 km depth: 26 GPa from 0 to 4 km depth, 30 GPa from 4 to 16 km, 33 GPa from 16 to 20 km and 39 GPa from 20 to 27 km, respectively. We compare this forward model prediction with that estimated from the Okada dislocation model and find that that the layered model produces only about 6 per cent less surface deformation than the homogeneous model (Fig. 5b, and Supporting Information Fig. S3, available in the electronic supplement). If we deepen the source by 3 km into the higher-rigidity layer, the model produces about 22 per cent less deformation than the homogeneous model and the M_w needed to match the observed amplitude increases by 0.1. Therefore,

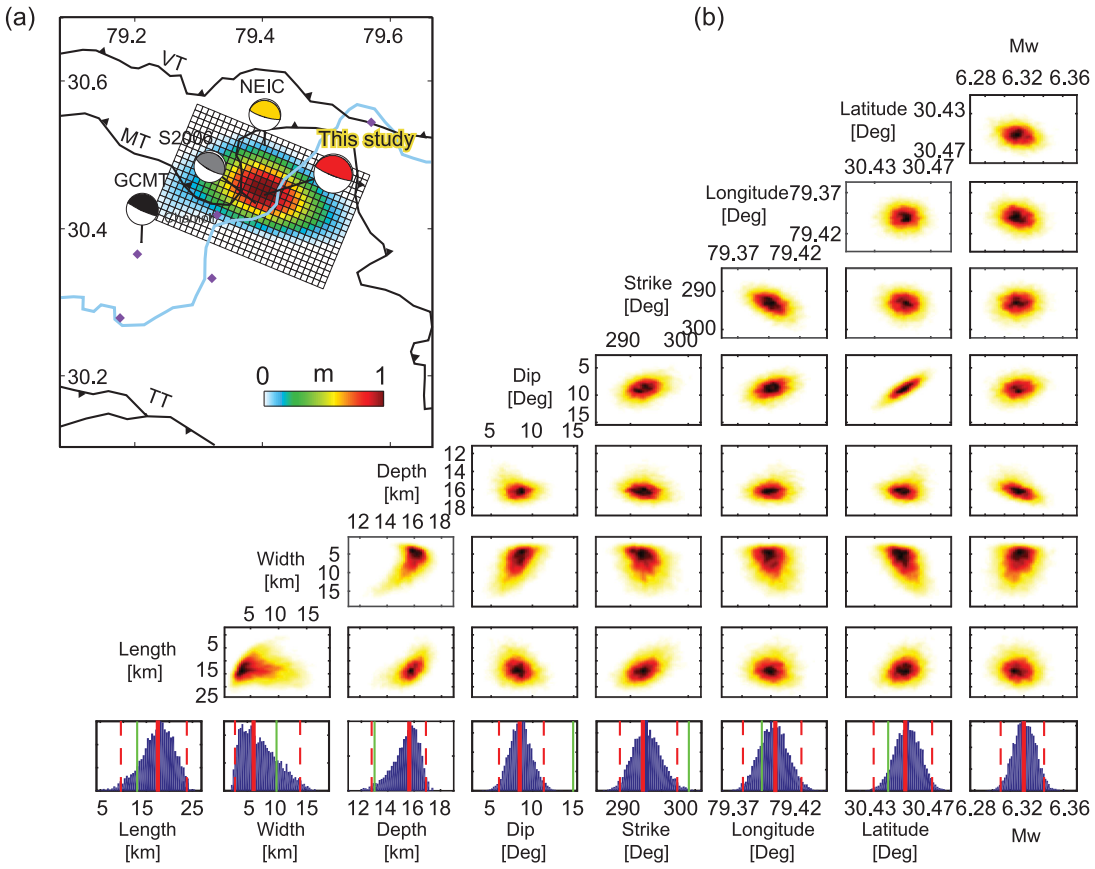

Figure 4. The spatial distribution of coseismic slip and uncertainties of the model parameters. (a) Slip distribution for a fault plane 30 km long, 20 km wide and dipping 9° NE (see location on Fig. 1), inverted from the ascending (Fig. 3) and descending (Fig. 2) InSAR data sets. The focal mechanisms indicating main-shock locations from the different catalogues and our study are shown. (b) Model parameter distribution. Rows 1–7: the 2-D distribution of parameter pairs. Possible trade-offs between parameters can be observed. Bottom row: histograms of model parameters: the best-fit model parameters are shown in thick red line with 95 per cent confidence interval bounds in red dashed lines. The green lines show the source parameters obtained by Satyabala & Bilham (2006).

Table 1 . Fault parameters for the 1999 Chamoli earthquake estimated from different data sets.

Reference	Lat. (°)	Long. (°)	Length (km)	Width (km)	Depth (km)	Strike (°)	Dip (°)	Rake (°)	Average slip (m)	M_w
NEIC	30.512	79.403	–	–	15	287	13	90	–	6.6
GCMT	30.38	79.21	–	–	15	280	7	75	–	6.5
S2006	30.44	79.39	13	10	13	300	15	90	0.55	6.2
This study	$30.45^{+0.02}_{-0.02}$	$79.40^{+0.02}_{-0.03}$	$17^{+6.3}_{-8.0}$	$6^{8.0}_{-3.2}$	$15.9^{+1.1}_{-3.0}$	$292^{+5.1}_{-3.4}$	$9^{+3.4}_{-2.2}$	90	0.5	$6.32^{+0.03}_{-0.02}$

Last two rows: longitude and latitude are for the centre of the fault plane, the depth is the centroid depth.
0.01° is roughly equal to 1 km at this latitude.

we think the use of the layered model does not greatly influence the M_w estimate of the Chamoli earthquake.

In addition, there are two other possible reasons that could explain the difference between the geodetic moment and seismic moment. First, for gently dipping pure thrust and normal faulting events, uncertainties in dips and moments are larger because of vanishing amplitudes of dip-slip Green's functions for shallower events in moment tensor inversions; second, the GCMT solution puts the source in the lower crustal layer of the PREM seismic velocity model (Vs = 3.9 km s^{-1}; $\mu = \sim 41$ GPa), whereas we assume $\mu = \sim 30$ GPa (Vs = 3.32 km s^{-1}). As the dip-slip Green's function amplitudes depend on Vs × Vs × density at the source. This difference in properties at the source alone would account for a factor of ∼1.5 difference in moments (Avinash Nayak, private communication, 2015).

The moment tensor solutions of the 1999 Chamoli main shock consistently show that the main shock has primarily thrust slip, except for the GCMT, which has a slightly oblique faulting mechanism. However, the strike, dip, focal depth and moment magnitude vary among solutions. According to the NEIC, the main shock occurred on a 13° north-dipping thrust at a fixed depth of 15 km striking N287°E (Table 1). The moment tensor solution given in the GCMT catalogue indicates thrust motion on the gently northward dipping nodal plane (strike N280°E, dip 7°, rake 75°). The dislocation solution estimated from previous InSAR observations suggests that the source fault has a strike of N300°E, dipping 15° towards north with a centroid depth of 13 km (Satyabala & Bilham 2006). Using the same SAR data with different data processing strategy, our fault plane is ∼2 km deeper, with a 4° shallower dip and is rotated 8° counter clockwise compared to the model fault obtained

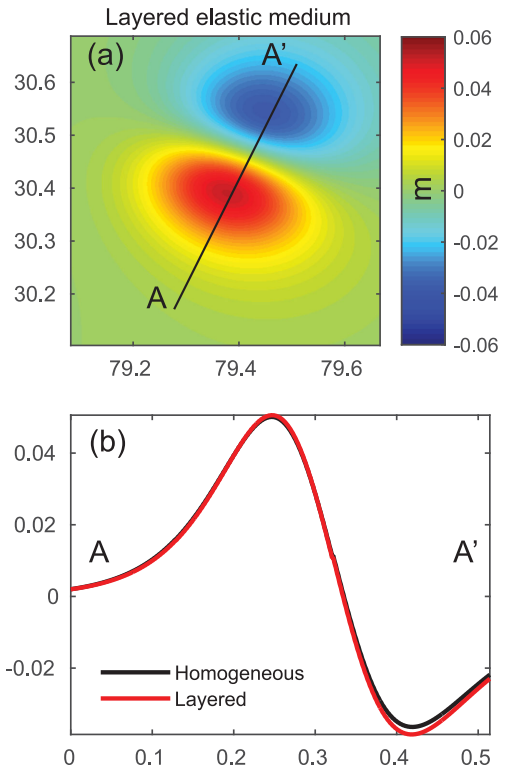

Figure 5. (a) Forward model prediction estimated from a layered elastic structure model using 1-D velocity model from Galetzka *et al.* (2015). (b) The difference between panel (a) and that from a homogeneous elastic earth structure model along profile A–A′.

by Satyabala & Bilham (2006). Our fault plane is located northeast of that derived by Satyabala & Bilham (2006). Since only the data constraint is estimated with a propagation of data errors without considering modelling errors (i.e. fault and medium model simplifications), our statistical confidence may be optimistic. Furthermore, the fixed values in all models (e.g. fixed depth in seismological models and fixed rake in geodetic models) can affect the estimated errors of other parameters. Relying on temporary network data, Rajput *et al.* (2005) examined a subset of 134 well-located aftershocks with depth errors within ± 3 km to better understand the rupture process. They found most of these aftershocks took place at depths shallower than 17 km with predominant thrust component (Kayal *et al.* 2003; Rajput *et al.* 2005). Therefore, we think a majority of the aftershocks recorded were concentrated above and near the up-dip edge of the rupture plane suggesting that they were due to the reactivation of minor thrust faults and did not represent the main process of seismic energy release. These shallow faults are not responsible for the 1999 Chamoli main shock and probably have less chance to generate great earthquakes (Kayal *et al.* 2003). Few aftershocks occurred beneath the fault plane or downdip of the main shock hypocentre, possibly due to the presence of fluid or high temperature at depth causing a transition from brittle faulting to stable sliding (Avouac 2003). Thus, we suggest that the locking line of the MHT in the Garhwal region may be located ∼120 km north of the surface trace of the MFT, at ∼17 km depth, which is consistent with other studies using different methods (Lemonnier *et al.* 1999; Caldwell *et al.* 2013).

5 CONCLUSIONS

We have used geodetic data to study the geometry and distribution of slip associated with the 1999 Chamoli earthquake. Our results demonstrate that the coseismic slip was produced by up to ∼1 m of thrust slip on a $9^{\circ}{}^{+3.4}_{-2.2}$ dipping fault. The rupture plane was located at depths between ∼15.2–17 km, on the northernmost detachment on the mid-crustal ramp of the MHT updip from the transition between aseismic shear and the locked detachment. The studies of the recent M_w 7.8 Gorkha, Nepal thrust faulting earthquake also show that coseismic slip may have extended down onto the ramp of the MHT (Elliott *et al.* 2016). Also, the Gorkha fault plane has a gentle dip and similar orientation to the 1999 Chamoli earthquake, implying that Himalayan earthquakes ($M_w > 6$) tend to occur along the same detachment surface on the MHT. The last great earthquake that has occurred within the Garhwal region was the 1505 M_w 8.2 earthquake (Bilham 2004). The 1999 Chamoli earthquake released seismic energy that is far less than the accumulated strain energy implying that the seismic hazard of the region remains high.

ACKNOWLEDGEMENTS

The work was partially supported by the National Natural Science Foundation of China (Nos 41222027 and 41474007) and the Hunan Provincial Natural Science Foundation of China (No. 13JJ1006). RB acknowledges funding from NSF award EAR-1014880. We thank the editor Jörg Renner, Roger Bilham and an anonymous reviewer for helpful comments. We thank Avinash Nayak and Doug Dreger for discussions and analysis of the earthquake magnitude estimates. WX thanks Renier Viltres for helping with the PSGRN/PSCMP package.

REFERENCES

Ader, T. *et al.*, 2012. Convergence rate across the Nepal Himalaya and interseismic coupling on the Main Himalayan Thrust: implications for seismic hazard, *J. geophys. Res.*, **117,** B04403, doi:10.1029/2011JB009071.

Avouac, J.P., 2003. Mountain building, erosion, and the seismic cycle in the Nepal Himalaya, *Adv. Geophys.*, **46,** 1–80.

Avouac, J.P., 2015. From geodetic imaging of seismic and aseismic fault slip to dynamic modeling of the seismic cycle, *Annu. Rev. Earth Planet. Sci.*, **43,** 233–271.

Avouac, J.P., Meng, L., Wei, S., Wang, T. & Ampuero, J.P., 2015. Lower edge of locked Main Himalayan Thrust unzipped by the 2015 Gorkha earthquake, *Nat. Geosci*., **8,** 708–711.

Banerjee, P. & Bürgmann, R., 2002. Convergence across the northwest Himalaya from GPS measurements, *Geophys. Res. Lett.*, **29**(13), doi:10.1029/2002GL015184.

Bilham, R., 2004. Earthquakes in India and the Himalaya: tectonics, geodesy and history, *Ann. Geophys.*, **47**(2–3), 839–858.

Bilham, R., Gaur, V.K. & Molnar, P., 2001. Himalayan seismic hazard, *Science,* **293**(5534), 1442–1444.

Caldwell, W.B., Klemperer, S.L., Lawrence, J.F. & Rai, S.S., 2013. Characterizing the Main Himalayan Thrust in the Garhwal Himalaya, India with receiver function CCP stacking, *Earth planet. Sci. Lett.*, **367,** 15–27.

Cattin, R. & Avouac, J.P., 2000. Modeling mountain building and the seismic cycle in the Himalaya of Nepal, *J. geophys. Res.*, **105**(B6), 13 389–13 407.

Célérier, J., Harrison, T.M., Webb, A.A.G. & Yin, A., 2009. The Kumaun and Garwhal Lesser Himalaya, India: Part 1. Structure and stratigraphy, *Bull. geol. Soc. Am.*, **121**(9–10), 1262–1280.

Cervelli, P., Murray, M.H., Segall, P., Aoki, Y. & Kato, T., 2001. Estimating source parameters from deformation data, with an application to the March 1997 earthquake swarm off the Izu Peninsula, Japan, *J. geophys. Res.*, **106**(B6), 11 217–11 237.

Chen, C.W. & Zebker, H.A., 2001. Two-dimensional phase unwrapping with use of statistical models for cost functions in nonlinear optimization, *J. Opt. Soc. Am. A,* **18,** 338–351.

Elliott, J.R., Jolivet, R., González, P.J., Avouac, J.-P., Hollingsworth, J., Searle, M.P. & Stevens, V.L., 2016. Himalayan megathrust geometry and relation to topography revealed by the Gorkha earthquake, *Nat. Geosci.,* **9,** 174–180.

Farr, T.G. *et al.*, 2007. The Shuttle Radar Topography Mission, *Rev. Geophys.,* **45,** RG2004, doi:10.1029/2005RG000183.

Feldl, N. & Bilham., R., 2006. Great Himalayan earthquakes and the Tibetan plateau, *Nature,* **444,** 165–170.

Feng, G., Li, Z. & Shan, X., 2015. Geodetic model of the April 25, 2015 M_w 7.8 Gorkha Nepal earthquake and M_w 7.3 aftershock estimated from InSAR and GPS data, *Geophys. J. Int.,* **203**(2), 896–900.

Galetzka, J. *et al.*, 2015. Slip pulse and resonance of Kathmandu basin during the 2015 M_w 7.8 Gorkha earthquake, Nepal, *Science,* **349**(6252), 1091–1095.

Grandin, R., Doin, M.P., Bollinger, L., Pinel-Puysségur, B., Ducret, G., Jolivet, R. & Sapkota, S.N., 2012. Long-term growth of the Himalaya inferred from interseismic InSAR measurement, *Geology,* **40**(12), 1059–1062.

Hearn, E.H. & Bürgmann, R., 2005. The effect of elastic layering on inversions of GPS data for earthquake slip and stress changes, *Bull. seism. Soc. Am.,* **95,** 1637–1653.

Jónsson, S., Zebker, H., Segall, P. & Amelung, F., 2002. Fault slip distribution of the 1999 M_w 7.1 Hector Mine, California, earthquake, estimated from satellite radar and GPS measurements, *Bull. seism. Soc. Am.,* **92**(4), 1377–1389.

Kayal, J.R., Ram, S., Singh, O.P., Chakraborty, P.K. & Karunakar, G., 2003. Aftershocks of the March 1999 Chamoli earthquake and seismotectonic structure of the Garhwal Himalaya, *Bull. seism. Soc. Am.,* **93**(1), 109–117.

Lavé, J. & Avouac, J.P., 2001. Fluvial incision and tectonic uplift across the Himalayas of central Nepal, *J. geophys. Res.,* **106**(B11), 26 561–26 591.

Lemonnier, C. *et al.*, 1999. Electrical structure of the Himalaya of central Nepal: high conductivity around the mid-crustal ramp along the MHT, *Geophys. Res. Lett.,* **26**(21), 3261–3264.

Li, Z.W., Ding, X.L., Huang, C., Zhu, J.J. & Chen, Y.L., 2008. Improved filtering parameter determination for the Goldstein radar interferogram filter, *ISPRS J Photogramm Remote Sens*., **63**(6), 621–634.

Lindsey, E., Natsuaki, R., Xu, X., Shimada, M., Hashimoto, H., Melgar, D. & Sandwell, D., 2015. Line-of-sight deformation from ALOS-2 interferometry: M_w 7.8 Gorkha earthquake and M_w 7.3 aftershock, *Geophys. Res. Lett.,* **42**(16), 6655–6661.

Mukhopadhyay, S. & Kayal, J.R., 2003. Seismic tomography structure of the 1999 Chamoli earthquake source area in the Garhwal Himalaya, *Bull. seism. Soc. Am.,* **93**(4), 1854–1861.

Ni, J. & Barazangi, M., 1984. Seismotectonics of the Himalayan collision zone: geometry of the underthrusting Indian plate beneath the Himalaya, *J. geophys. Res.,* **89**(B2), 1147–1163.

Okada, Y., 1985. Surface deformation due to shear and tensile faults in a half-space, *Bull. seism. Soc. Am.,* **75**(4), 1135–1154.

Qiao, X., Ren, S., Nie, Z., Zhou, Y., Shen, Q. & Yang, S., 2010. Study on crustal deformation of the M_s 6.6 Damxung earthquake in 2008 by InSAR measurements, *J. Geod. Geodyn.,* **1**(1), 15–22.

Rajendran, C.P., John, B. & Rajendran, K., 2015. Medieval pulse of great earthquakes in the central Himalaya: viewing past activities on the frontal thrust, *J. geophys. Res.,* **120,** 1623–1641.

Rajput, S., Gahalaut, V.K., Raju, P.S. & Kayal, J.R., 2005. Rupture parameters of the 1999 Chamoli earthquake in Garhwal Himalaya: constraints from aftershocks and change in failure stress, *Tectonophysics,* **404**(1), 23–32.

Sarkar, I., Pachauri, A.K. & Israil, M., 2001. On the damage caused by the Chamoli earthquake of 29 March, 1999, *J. Asian Earth Sci.,* **19**(1), 129–134.

Satyabala, S.P. & Bilham, R., 2006. Surface deformation and subsurface slip of the 28 March 1999 M_w = 6.4 west Himalayan Chamoli earthquake from InSAR analysis, *Geophys. Res. Lett.,* **33,** L23305, doi:10.1029/2006GL027422.

Stevens, V.L. & Avouac, J.P., 2015. Interseismic coupling on the Main Himalayan Thrust, *Geophys. Res. Lett.,* **42,** 5828–5837.

Sudhaus, H. & Jónsson, S., 2009. Improved source modelling through combined use of InSAR and GPS under consideration of correlated data errors: application to the June 2000 Kleifarvatn earthquake, Iceland, *Geophys. J. Int.,* **176**(2), 389–404.

Wang, K. & Fialko, Y., 2015. Slip model of the 2015 M_w 7.8 Gorkha (Nepal) earthquake from inversions of ALOS-2 and GPS data, *Geophys. Res. Lett.,* **42,** 7452–7458.

Wang, R., Lorenzo-Martin, F. & Roth, F., 2006. PSGRN/PSCMP-a new code for calculating co-postseismic deformations and geopotential changes based on the viscoelastic-gravitational dislocation theory, *Comput. Geosci.,* **32,** 527–541.

Weston, J., Ferreira, A.M.G. & Funning, G.J., 2011. Global compilation of interferometric synthetic aperture radar earthquake source models: 1. Comparisons with seismic catalogs, *J. geophys. Res.,* **116,** B08408, doi:10.1029/2010JB008131.

Wobus, C., Heimsath, A., Whipple, K. & Hodges, K., 2005. Active out-of-sequence thrust faulting in the central Nepalese Himalaya, *Nature,* **434**(7036), 1008–1011.

Xu, W., Dutta, R. & Jónsson, S., 2015. Identifying active faults by improving earthquake locations with InSAR data and Bayesian estimation: the 2004 Tabuk (Saudi Arabia) earthquake sequence, *Bull. seism. Soc. Am.,* **105**(2A), 765–775.

Xu, W.B. *et al.*, 2010. Correcting Atmospheric Effects in ASAR interferogram with MERIS Integrated Water Vapor Data, *Chin. J. Geophys.,* **53**(5), 1073–1084.

Yin, A., 2006. Cenozoic tectonic evolution of the Himalayan orogen as constrained by along-strike variation of structural geometry, exhumation history, and foreland sedimentation, *Earth-Sci. Rev.,* **76**(1), 1–131.

SUPPORTING INFORMATION

Additional Supporting Information may be found in the online version of this paper:

Figure S1. Comparison between the original interferogram (left column) and the unwrapped and then rewrapped interferograms (right column). The top row shows the ascending data and the bottom row the descending data.

Figure S2. Covariance (black) and fitted covariance functions (red) of the noise in (a) the ascending data and (b) the descending data.

Figure S3. (a) Forward model predictions estimated from a homogeneous elastic earth structure model. (b) The difference between Fig. 5(a) and panel (a) (http://gji.oxfordjournals.org/lookup/suppl/doi:10.1093/gji/ggw016/-/DC1).

Please note: Oxford University Press is not responsible for the content or functionality of any supporting materials supplied by the authors. Any queries (other than missing material) should be directed to the corresponding author for the paper.